

Article

Greenhouse Gas Conversion into Hydrocarbons and Oxygenates Using Low Temperature Barrier Discharge Plasma Combined with Zeolite Catalysts

Oleg V. Golubev ^{*}, Dmitry E. Tsaplin and Anton L. Maximov 

A.V. Topchiev Institute of Petrochemical Synthesis, Russian Academy of Sciences (TIPS RAS), Moscow 119991, Russia

^{*} Correspondence: golubev@ips.ac.ru

Abstract: Global warming occurs as a result of the build-up of greenhouse gases in the atmosphere, causing an increase in Earth's average temperature. Two major greenhouse gases (CH₄ and CO₂) can be simultaneously converted into value-added chemicals and fuels thereby decreasing their negative impact on the climate. In the present work, we used a plasma-catalytic approach for the conversion of methane and carbon dioxide into syngas, hydrocarbons, and oxygenates. For this purpose, CuCe zeolite-containing catalysts were prepared and characterized (low-temperature N₂ adsorption, XRF, XRD, CO₂-TPD, NH₃-TPD, TPR). The process of carbon dioxide methane reforming was conducted in a dielectric barrier discharge under atmospheric pressure and at low temperature (under 120 °C). It was found that under the studied conditions, the major byproducts of CH₄ reforming are CO, H₂, and C₂H₆ with the additional formation of methanol and acetone. The application of a ZSM-12 based catalyst was beneficial as the CH₄ conversion increased and the total concentration of liquid products was the highest, which is related to the acidic properties of the catalyst.

Keywords: carbon dioxide utilization; greenhouse gases emissions; plasma catalysis; dry methane reforming; zeolites



Citation: Golubev, O.V.; Tsaplin, D.E.; Maximov, A.L. Greenhouse Gas Conversion into Hydrocarbons and Oxygenates Using Low Temperature Barrier Discharge Plasma Combined with Zeolite Catalysts. *Gases* **2023**, *3*, 165–180. <https://doi.org/10.3390/gases3040012>

Academic Editors: Paola Ammendola and Ben J. Anthony

Received: 18 August 2023

Revised: 23 November 2023

Accepted: 4 December 2023

Published: 5 December 2023



Copyright: © 2023 by the authors. Licensee MDPI, Basel, Switzerland. This article is an open access article distributed under the terms and conditions of the Creative Commons Attribution (CC BY) license (<https://creativecommons.org/licenses/by/4.0/>).

1. Introduction

The accumulation of greenhouse gases in the Earth's atmosphere has become a prominent environmental concern in recent decades due to its profound impact on our planet's atmosphere and climate. Greenhouse gases, such as carbon dioxide, methane, nitrous oxide, and fluorinated gases, play a crucial role in regulating the Earth's temperature through the greenhouse effect. However, human activities (burning of fossil fuels, deforestation, and industrial processes) have significantly increased the concentration of these gases, leading to a disbalance in the natural climate system. Consequently, the concentration levels of CO₂ and other greenhouse gases have reached unprecedented levels in the last century [1].

The joint processing of greenhouse gases, specifically methane and carbon dioxide, can be advantageous in terms of greenhouse gas reduction, energy, fuels and chemicals production [2,3]. One of the main methods to convert both methane and carbon dioxide in a single process is the dry methane reforming (DRM) process [4,5]. Dry methane reforming offers numerous opportunities for the production of valuable intermediates and chemicals. The product of this reaction is a syngas, which consists of CO and H₂. The resulting syngas can be further processed to obtain various fuels and chemicals. For example, Fischer-Tropsch synthesis can convert syngas into synthetic hydrocarbons such as gasoline, diesel, and waxes. Alternatively, the syngas can serve as a precursor for the production of methanol, ammonia, or other chemical compounds [6,7]. However, there are some limitations regarding DRM. The reaction is highly endothermic and requires elevated temperatures for efficient conversion. Carbon deposition is also a common issue, where carbonaceous species can accumulate on the surface of the catalyst, leading to

catalyst deactivation [4]. Therefore, effective catalyst design and reactor engineering are crucial to prevent carbon deposition and maintain catalytic activity over extended periods. Traditionally, transition metals like Ni or Co are widely studied in DRM due to their availability and low cost [8,9]. However, its coking resistance ability is relatively low, so numerous catalyst modification attempts are being made. For example, Ni-Co bimetallic mullite catalysts [10], Zr-La-Ti oxide catalysts [11], as well as Ga-doped Ni/CeO₂ [12] are reported to show remarkable stability against carbon deposition. As an alternative to thermal-induced dry methane reforming, photocatalytic [13,14] and photo-thermal [15] DRM show great potential for reducing process temperature and enhancing gas conversion.

Another way to overcome the limitations of thermal-catalytic DRM is a plasma-catalytic approach [16]. This process combines the advantages of plasma technology and catalysis to enhance the efficiency and selectivity of the reforming reaction [17]. Plasma can activate the reactant molecules, enhancing their reactivity, and reducing the energy barrier for the reactions. The main advantage of non-thermal plasma is that it makes it possible to conduct thermodynamically unfavorable reactions at low temperatures due to the non-equilibrium character of plasma [18]. In comparison to thermal-activated processes, in non-thermal plasma, the vibrational excitation and the energy transfer from one active species (i.e., electron, ion, radical) to the neutral molecule are the main pathways of molecule activation [19]. The presence of the catalyst helps to improve overall reaction efficiency by providing active sites for the adsorption and activation of reactant molecules. Additionally, plasma can regenerate the catalyst by removing deposited carbon species, thus extending its lifetime.

One of the attractive ways to tune plasma-catalytic dry methane reforming is to use the process not only for syngas production but for oxygenate production via a single-stage process [20–24]. In order to achieve that, the selection of the catalyst should be carefully performed. In the dry methane reforming reaction, methane decomposition occurs on the acidic part of the support [25], so one of the requirements for the catalyst support is the presence of acid centers on the surface. The most commonly used materials for supports are Al₂O₃, SiO₂, and zeolites, which may be modified by TiO₂, ZrO₂, and CeO₂ [20,26–28]. Zeolites are structured aluminosilicates, which possess acid properties, and the acidity may be widely varied. With the variation of the acidity in the catalyst, different reaction products can be obtained. For example, a higher concentration of Brønsted acid centers in an HZSM-5-based catalyst for plasma-catalytic DRM leads to the formation of acetic acid, while a catalyst with less acidic properties exhibits higher activity towards methanol formation [29]. As previously stated [30], the course of the reaction is also affected by the presence of oxygen vacancies on the surface; in particular, the addition of magnesium-aluminum oxide to the catalyst increases CO₂ conversion due to the formation of the oxygen vacancies. As reported in the literature [31,32], the textural properties of the supports are important as microporosity inhibits the formation of micro discharges inside the pores and thus decreases the conversion. Regarding the active phase, such metals as Ni, Co, Mo, V, Na, Cu, Zn, Pt, Ag, or their combination [33] are commonly used [34–36]. It is reported that the adsorption and dissociation of methyl radicals and their subsequent recombination with other particles is particularly effective on copper and zinc centers [29,37–39]. The advantage of Cu-based catalysts in plasma-catalytic dry methane reforming is attributed to high activity in C–H bond splitting in CH₄ and the subsequent C–C coupling resulting in a higher oxygenate yield [40].

In the present study, we aimed to compare the activity of zeolite-based Cu catalysts for plasma-catalytic dry methane reforming. A zeolite of the MTW (ZSM-12) type was chosen for comparison with the widely used MFI (ZSM-5) zeolite due to its unique porous structure and tuning acidity availability [41]. To the best of our knowledge, the MTW-type zeolite was not studied in plasma-catalytic dry methane reforming so far by other researchers. The zeolites were combined with Al₂O₃ in order to increase the porous characteristics and to create a shaped body catalyst. A preliminary study was made by our group [42], where Ni- and Co-ZSM-12 based catalysts showed better plasma-catalytic performance compared to

ZSM-5-based catalysts. In the current research, we focus on the Cu-containing catalysts and the evaluation of their activity and stability in the plasma-catalytic dry methane reforming process.

2. Materials and Methods

The reagents, which were used for the preparation of the catalysts, are summarized in Table 1. All the reagents were used without further purification.

Table 1. Reagents used for catalyst preparation.

Reagent	Purity	Manufacturer
colloid silica Ludox HS-40	40 wt% solution	Sigma-Aldrich, St. Louis, MO, USA
$\text{Al}_2(\text{SO}_4)_3 \cdot 18\text{H}_2\text{O}$	98%	Sigma-Aldrich
N-Methyldiethanolamine	99%	Sigma-Aldrich
bromoethane	99%	Sigma-Aldrich
NaOH	>97%	LLC "Komponent-Reaktiv", Moscow, Russia
NH_4Cl	98%	Reachem, Chennai, India
boehmite Pural SB	99%	Sasol, Hamburg, Germany
ZSM-5 zeolite	>90%	JSC "NZHK", Novosibirsk, Russia
HNO_3	65 wt% solution	LLC "NevaReaktiv", Saint-Petersburg, Russia
$\text{Ce}(\text{NO}_3)_2 \cdot 6\text{H}_2\text{O}$	99%	LLC "Tsent Tekhnologii Lantan", Moscow, Russia
$\text{Cu}(\text{NO}_3)_2 \cdot 3\text{H}_2\text{O}$	99.9%	JSC "Lenreaktiv", Saint-Petersburg, Russia

2.1. Preparation of the Catalysts

The synthesis of the ZSM-12 zeolite was conducted according to the procedure reported before by our group [43]. In a typical synthesis, a gel was prepared by mixing the solutions of $\text{Al}_2(\text{SO}_4)_3 \cdot 18\text{H}_2\text{O}$, NaOH, N-Methyldiethanolamine, and a colloid silica solution. The obtained gel was further hydrothermally treated at 155 °C for 120 h, then washed, dried, and calcined. After several cycles of an ion-exchange procedure, an H-form of the ZSM-12 zeolite was obtained.

For the preparation of the catalyst support, the obtained ZSM-12 zeolite and a commercial ZSM-5 zeolite were used. Boehmite (AlOOH) was used as a binder to obtain a shaped body support. The ratio of zeolite-to-binder was 70/30 by mass. A portion of boehmite (10.7 g) was mixed with 25 g of zeolite, then ground in a mortar to obtain a homogeneous mixture. After that, HNO_3 (21 cm³, 1 M) was added until a viscous mass was formed. The mass was further extruded, dried (60 °C for 2 h, 80 °C for 2 h, 110 °C for 2 h), and calcined (550 °C for 4 h). The obtained granules of support were additionally chopped to a size of 0.8–1.5 cm. Based on the zeolite used, two supports were obtained which were designated as ZSM-5/ Al_2O_3 and ZSM-12/ Al_2O_3 .

The catalyst support was impregnated with a solution of $\text{Cu}(\text{NO}_3)_2 \cdot 3\text{H}_2\text{O}$ and $\text{Ce}(\text{NO}_3)_2 \cdot 6\text{H}_2\text{O}$ salts with further drying and calcination. The catalyst supported on the ZSM-5/ Al_2O_3 support was designated as CuCe-5 and the catalyst supported on the ZSM-12/ Al_2O_3 support was designated as CuCe-12. Prior to the plasma-catalytic experiments, the catalysts were reduced in H_2 flow at 400 °C for 2 h.

2.2. Catalysts Characterization

The specific surface area, pore volume, and pore diameter of the prepared supports and the catalysts were determined by low-temperature N_2 adsorption analysis using a Belsorp miniX (Microtrac MRB, Osaka, Japan) surface area and pore size distribution analyzer. Before analysis, the catalysts (supports) were thermally degassed for 8 h ($T = 300$ °C, $p = 10$ Pa). The Brunauer–Emmett–Teller method was used for specific surface area calculation at $p/p_0 = 0.05$ –0.2.

The elemental composition of the catalysts was determined by X-ray fluorescent spectroscopy using an ARL Perform's Sequential (Thermo Fisher Scientific, Ecublens, Switzer-

land) analyzer (X-ray tube power is 2500 W). The sample, before analysis, was ground and pressed into a tablet with H_3BO_3 .

The X-ray diffraction patterns were registered with a range of $2\theta = 10^\circ\text{--}90^\circ$ using a Rigaku Rotaflex RU-200 (Tokyo, Japan) diffractometer ($\text{CuK}\alpha$ radiation) equipped with a Rigaku D/Max-RC goniometer (a rotation speed of $1^\circ/\text{min}$; a step 0.04°). The diffractograms were identified using the PDF-2 ICDD database.

The average size (D) of crystallites was calculated using the Scherrer equation:

$$D = \frac{K\lambda}{\beta \cos\theta} \quad (1)$$

where D is the crystallite size, λ is the wavelength of the $\text{Cu-K}\alpha$ radiation, K is a constant and its value is taken as 0.9, θ is the diffraction angle (rad), and β is the full-width at half maximum (FWHM) (rad).

The acidity of the samples was measured by NH_3 temperature-programmed desorption (NH_3 -TPD) using a USGA-101 (LLC "Unisit", Moscow, Russia) device. The sample ($m = 0.15\text{--}0.2$ g) was treated in He flow in order to purify the surface from the adsorbed water and oxygen ($T = 512^\circ\text{C}$ for 40 min). Then, the sample was saturated with NH_3 (5 vol% NH_3 —95 vol% He) at 60°C for 24 min. The analysis was conducted in helium flow at $100\text{--}800^\circ\text{C}$ (heating rate $7^\circ\text{C}/\text{min}$). Desorbed NH_3 registration was carried out using a thermal conductivity detector. The TPD profiles were deconvoluted using PeakFit (v4.12) software.

The temperature-programmed reduction of the catalysts was carried out using a USGA-101 device. Prior to analysis, the sample was calcined at 500°C for 30 min in Ar flow, then cooled down to 60°C . The reduction of the sample was conducted at the $10^\circ\text{C}/\text{min}$ rate up to 950°C .

2.3. Plasma-Catalytic Gases Utilization

The process of carbon dioxide methane reforming was studied using a plasma-catalytic dielectric barrier discharge reactor unit (Figure 1). The mixture of CH_4 and CO_2 was fed into the reactor using RRG-20 precise mass-flow controllers (LLC "Eltochpribor", Zelenograd, Russia). The flow rate of the gases was set to 23.5 mL/min each and the total gas flowrate was 47 mL/min. A dielectric barrier discharge was formed in a quartz tube (16 mm outer diameter, 2 mm wall thickness) between the two electrodes. A steel rod (8 mm diameter) with a tread was placed inside the reactor (inner electrode) and a steel mesh (0.5 mm mesh size, 80 mm length) was placed on the outer wall of the quartz tube (ground electrode). The catalyst (1 g) was placed between the inner electrode and the inner wall of the tube and was fixed with mineral wool at both ends of the packed bed. A high voltage generator had a sine wave signal with a frequency of 23 kHz and was connected to the inner electrode. The electric signals were registered using a Tektronix TDS 2012B oscilloscope (Tektronix, Beaverton, OR, USA). Each experiment was conducted for 2 h with a gradual increase of voltage from 3.5 to 4.8 kV.

Based on the Volt–Columb characteristics of the discharge (Lissajous figure), the plasma absorbed power was calculated according to the equation:

$$P = fW = fC_n A, \quad (2)$$

where C_n is the value of the capacitor included in series with the discharge tube, f is a frequency of the applied voltage, and A is the area of a Lissajous figure.

The energy efficiency of the process (η) was calculated as a ratio of converted gas (CH_4 or CO_2) to the absorbed power using the following equation:

$$\eta \left(\text{mmol} \times \text{kJ}^{-1} \right) = \frac{\nu_{\text{conv}}}{P} \times \frac{1000}{60}, \quad (3)$$

where ν_{conv} is the quantity of the gas converted (mol/min) and P is the absorbed power (W).

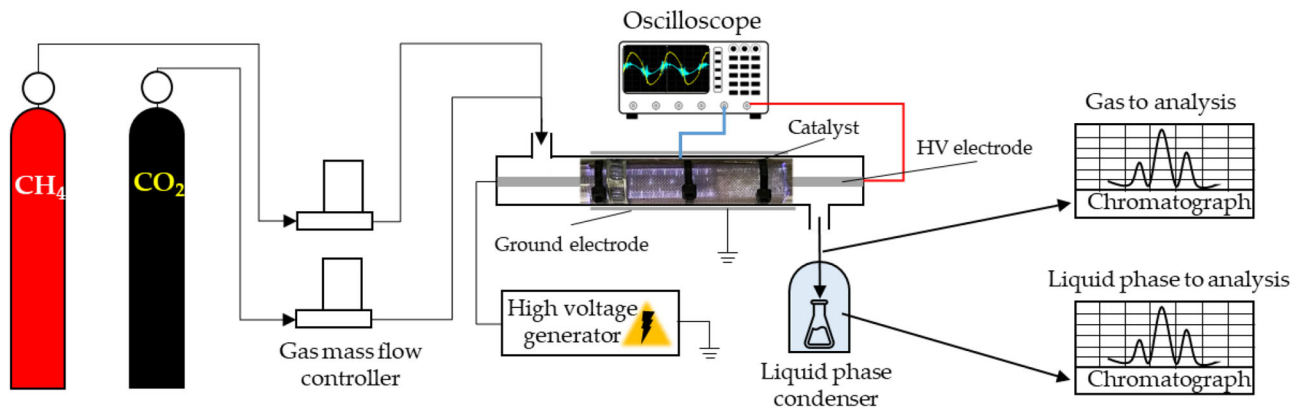


Figure 1. Scheme of the plasma-catalytic unit.

The gaseous outlet mixture was analyzed using a PIA gas chromatograph (LLC “NPF MEMS”, Samara, Russia) with a thermal conductivity detector and equipped with a Hayesep N adsorbent column ($l = 2$ m) for the determination of CO_2 and C_2H_6 and a molecular sieve 13 Å column ($l = 2$ m) for the determination of H_2 , CO , CH_4 . The content of the gases was calculated based on the calibration curves.

Liquid products were trapped in an ice-chilled vessel which contained 20 mL of distilled water. The product flow from the reactor outlet bubbled through the vessel, so the liquid products were dissolved in water. The obtained solution was analyzed using a Crystallux-4000M (RPC “META-CHROM”, Yoshkar-Ola, Russia) gas chromatograph with a Poraplot Q capillary column (25 m \times 0.53 mm).

Based on the data obtained during the chromatographic analysis, the conversion (X), product selectivity (S), and product yield (Y) were calculated according to the equations:

$$X_{\text{CO}_2}(\%) = \frac{v_{\text{CO}_2(\text{in})} - v_{\text{CO}_2(\text{out})}}{v_{\text{CO}_2(\text{in})}} \times 100\% \quad (4)$$

$$X_{\text{CH}_4}(\%) = \frac{v_{\text{CH}_4(\text{in})} - v_{\text{CH}_4(\text{out})}}{v_{\text{CH}_4(\text{in})}} \times 100\% \quad (5)$$

$$S_{\text{CO}}(\%) = \frac{v_{\text{CO}(\text{prod})}}{v_{\text{CO}_2(\text{conv})} + v_{\text{CH}_4(\text{conv})}} \times 100\% \quad (6)$$

$$S_{\text{H}_2}(\%) = \frac{v_{\text{H}_2(\text{prod})}}{2 \times v_{\text{CH}_4(\text{conv})}} \times 100\% \quad (7)$$

$$S_{\text{C}_2\text{H}_6}(\%) = \frac{v_{\text{C}_2\text{H}_6(\text{prod})}}{v_{\text{CO}_2(\text{conv})} + v_{\text{CH}_4(\text{conv})}} \times 100\% \quad (8)$$

$$Y_{\text{CO}}(\%) = \frac{v_{\text{CO}(\text{prod})}}{v_{\text{CO}_2(\text{in})} + v_{\text{CH}_4(\text{in})}} \times 100\% \quad (9)$$

$$Y_{\text{H}_2}(\%) = \frac{v_{\text{H}_2(\text{prod})}}{2 \times v_{\text{CH}_4(\text{in})}} \times 100\% \quad (10)$$

where $v_{(\text{in})}$ is the quantity of gas (CO_2/CH_4) which was injected into the reactor (mol), $v_{(\text{out})}$ is the quantity of the gas in the outlet stream (mol), $v_{(\text{prod})}$ is the quantity of the gas produced (mol), $v_{(\text{conv})}$, and is the quantity of the gas (CO_2/CH_4) which was converted to the products during the reaction.

3. Results and Discussion

3.1. Zeolite Catalyst Synthesis and Characterization

The prepared catalyst supports and the impregnated catalysts were analyzed with various methods to investigate their physicochemical characteristics. According to the low-temperature N₂ adsorption, the prepared zeolite supports had a relatively high specific surface area, which decreased slightly after the addition of the metals (Table 2). The pore volume was the same as in the support in case of the CuCe-5 and the CuCe-12 samples, which can indicate that the metal oxides were mostly located on the surface of the support rather than inside the pores.

Table 2. Elemental composition and the textural characteristics of the obtained supports and catalysts.

Sample	Elemental Composition, wt%				Textural Characteristics		
	Al	Si	Ce	Cu	S _{BET} , m ² /g	V _{pores} , cm ³ /g	d _{pores} , nm
ZSM-5/Al ₂ O ₃	15.7	32.7	-	-	287	0.21	6.1
CuCe-5	13.0	30.3	3.4	4.6	250	0.21	6.4
ZSM-12/Al ₂ O ₃	12	36	-	-	181	0.19	9.1
CuCe-12	10.6	32.3	3.8	4.5	147	0.18	10.2

The studied adsorption isotherms of the ZSM-5 and ZSM-12 zeolites (Figure 2) according to the IUPAC classification belong to type I isotherms, which indicates the microporosity of the zeolites. The adsorption isotherms of the ZSM-5/Al₂O₃ and ZSM-12/Al₂O₃ supports as well as the CuCe-5 and CuCe-12 catalysts also belong to type I in the range of low relative pressures, and to isotherm IV in the range of high relative pressures. Thus, the supports and the catalysts contain both micro- and mesopores. The presence of the mesopores is explained by the addition of Al₂O₃ in order to form a shaped body catalyst.

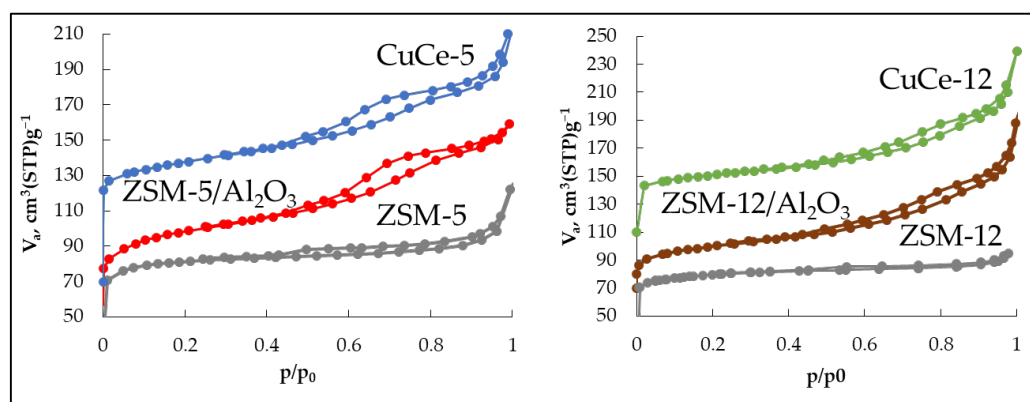


Figure 2. Low-temperature N₂ adsorption isotherms of the zeolites, supports, and catalysts.

The pore size distribution of the supports and the catalyst is shown on Figure 3. For each sample, two peaks are present on the graph. The peak at 3.9 nm does not reflect the actual porous characteristics of the samples, and corresponds to the tensile strength effect, which is determined by the properties of the adsorptive [44]. Thus, only the peaks at 5.7 nm (for ZSM-5-based samples) and 6.7 nm (for ZSM-12-based samples) are taken into consideration. It can be seen from the plots that the ZSM-5-based samples have a narrower pore size distribution: the average pore diameter (6.1 nm for ZSM-5/Al₂O₃ and 6.4 nm for CuCe-5) is close to the data from the BJH plot. For the ZSM-12 based samples, the pore size distribution is wider (peak at 6.7–7.0 nm), which means a less uniform distribution (average pore size 9.1–10.2 nm).

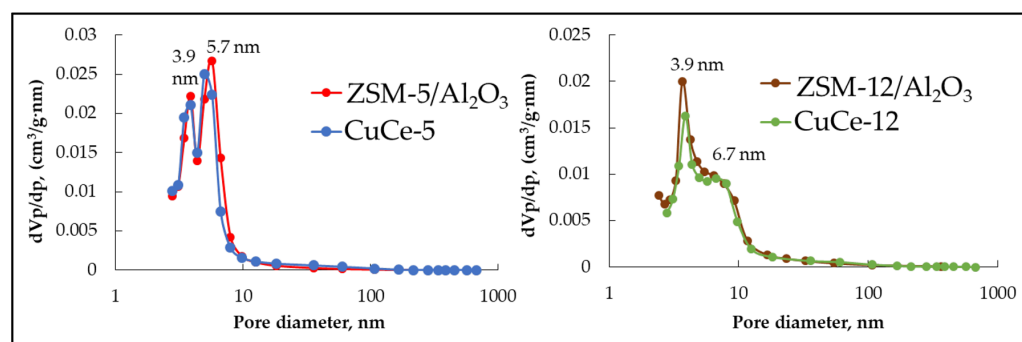


Figure 3. Pore size distribution based on desorption branch of the BJH plot.

The acidity of the samples was determined by temperature-programmed NH_3 desorption. It was stated that the ZSM-5-based samples had more acid sites, which is attributed to Si/Al ratio in the parent zeolites. As the Si/Al ratio tends to diminish (as in the ZSM-5 zeolite case), the acidity increases (Table 3). The TPD-patterns were deconvoluted to obtain three desorption peaks: the low-temperature (200–210 °C), the moderate-temperature (~250 °C) and the high-temperature peak at ~400 °C (Figure 4). According to the literature [45], the low-temperature peak can be ascribed to physically adsorbed ammonia (weak acid sites), so the true acid sites (medium and strong acid sites) can be described by the moderate- and high-temperature peak. It can be seen from the figure that with the addition of Cu and Ce to the support, the medium-temperature peak is shifted towards higher temperature and the area peak is increased compared to that in the TPD pattern of the corresponding supports. This can be related to the effect of the sequential desorption of the NH_3 which is attached to Cu ions [46].

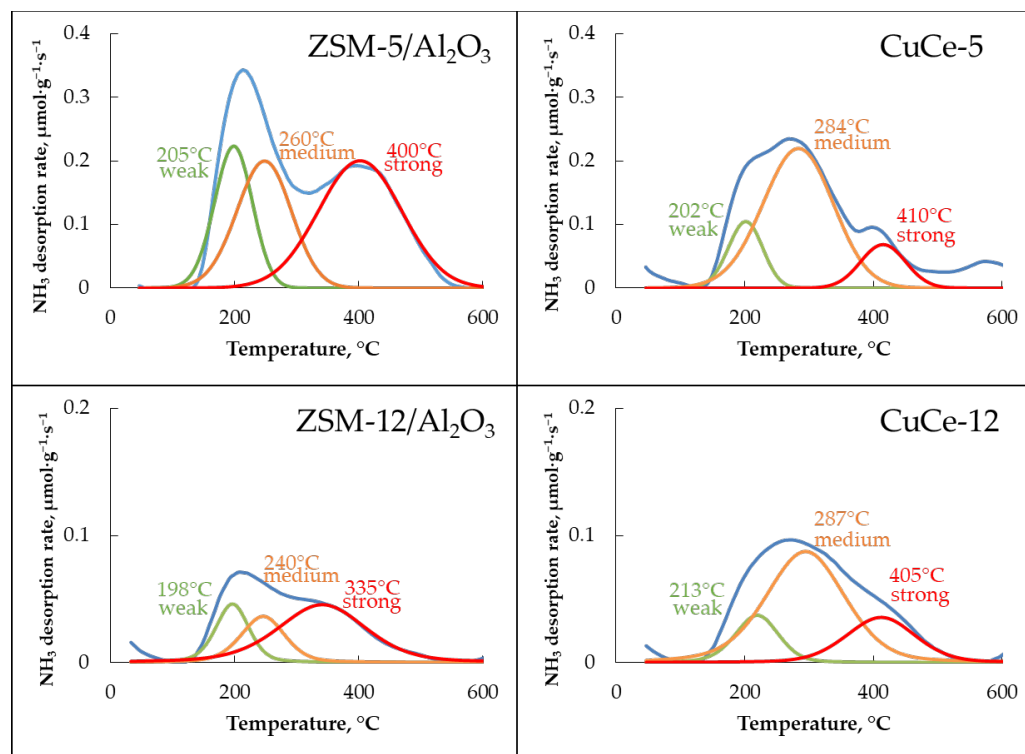
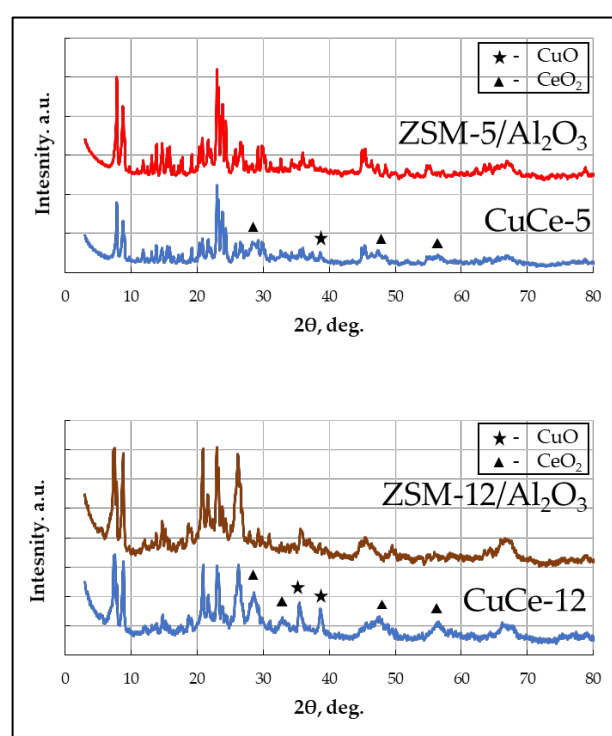


Figure 4. NH_3 -TPD profiles of the prepared supports and catalysts.

Table 3. Quantity of the acid sites determined by NH₃-TPD.

Sample	Acid Site Concentration, $\mu\text{mol/g}$			Total
	Weak Sites ~200 °C	Medium Sites ~250 °C	Strong Sites ~400 °C	
ZSM-5/Al ₂ O ₃	118	159	254	531
CuCe-5	49	223	45	317
ZSM-12/Al ₂ O ₃	23	25	65	113
CuCe-12	24	106	38	168

On the X-ray diffractograms, it can be seen that the zeolite structure was not destroyed during metal loading (Figure 5). The diffraction patterns in the range of $2\theta = 5^\circ\text{--}30^\circ$ are attributed to the zeolite phase and the intensity of these patterns does not change significantly.

**Figure 5.** X-ray diffractograms of the supports and obtained catalysts.

The average size of the crystallites was determined for the CeO₂ and CuO phases (Table 4). It should be noted that the CuO phase in CuCe-5 sample is not distinguished, which may be the result of the high dispersion of that phase on the ZSM-5/Al₂O₃ support surface. This support has a higher specific surface area, which leads to a better particle distribution. However, CeO₂ crystallites are of a similar size in both catalysts, which indicates no effect of the support properties on the CeO₂ crystallite size.

Table 4. The average crystallite size of the CeO₂ and CuO phases.

Catalyst	Phase	Crystallite Size, nm
CuCe-5	CeO ₂	4.4 ± 0.5
	CuO	n/d *
CuCe-12	CeO ₂	4.6 ± 0.4
	CuO	18.3 ± 0.5

* n/d = no data.

The temperature-programmed H_2 reduction of the obtained samples was conducted in order to investigate the reducibility of the catalysts prior to the plasma-catalytic experiments. The reduction temperature of the pure CuO is in the range of 300–400 °C depending on the analysis conditions, as reported in the literature [47]. The reduction of pure CeO_2 is observed in a temperature range of 350–580 °C and above 900 °C [48,49]. It is seen from the TPR profiles (Figure 6) that the reduction temperature is lower than that of the pure CuO and CeO_2 substances. In the literature, it is stated that $CuO-CeO_2$ systems have a lower reduction temperature because of the interaction of the two oxides [50]. In the TPR pattern of the CuCe-5 sample, only one high-intensity peak is present, which may indicate higher CuO particle dispersion [51], which confirms the XRD results. The TPR pattern of the CuCe-12 differs from the one of CuCe-5 and three peaks are distinguished in the TPR profile. According to the literature [52], the low-temperature peak (~150 °C) is attributed to the reduction of CuO_x , which interacts strongly with CeO_2 , the peak at ~210 °C is attributed to the reduction of highly dispersed CuO_x particles on the surface, and the high-temperature peak (~260 °C) is attributed to bulk CuO_x particles. The latter is also consistent with the CuO crystallite size data obtained by the XRD analysis.

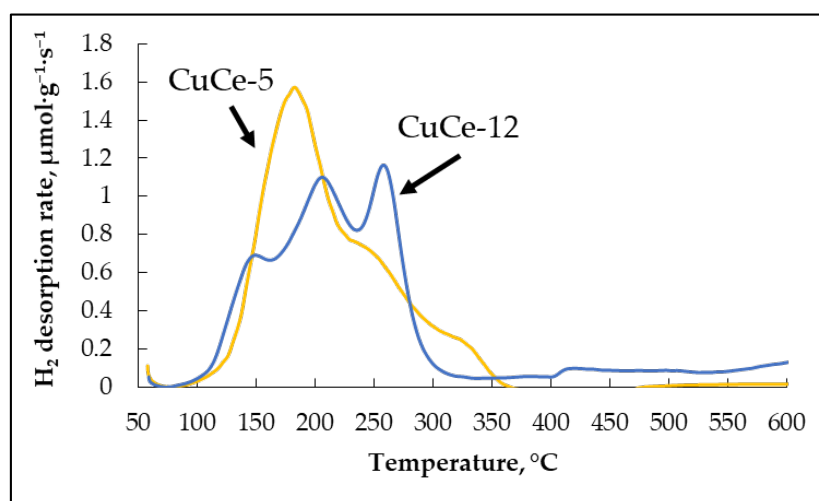


Figure 6. Temperature programmed reduction profiles of the CuCe-5 and CuCe-12 samples.

3.2. Gas Conversion Using Plasma-Catalytic Process

In order to test the activity of the prepared catalysts, a dielectric barrier discharge plasma reactor was used. As a blank test, an experiment in an empty reactor without a catalyst was conducted. On Figure 7, the Lissajous figures, which were registered during the blank test, are presented.

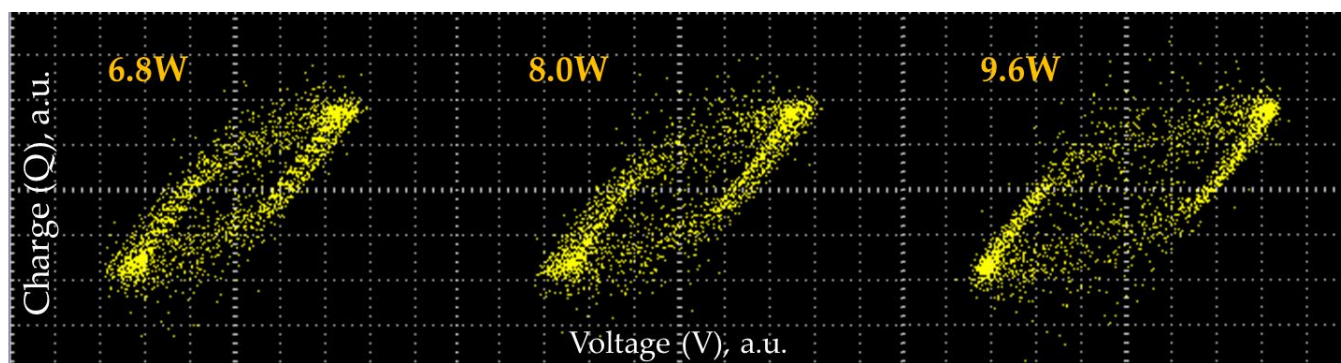


Figure 7. Lissajous figure evolution during the power increase in a blank experiment (empty reactor, $CH_4:CO_2 = 1:1$, total gas flow 47 mL/min).

It can be seen that with the increase in the input power, the shape of the figure (parallelogram) remains unchanged, but the figure itself is broadened, which is due to enhanced voltage and current signals. The observed shape of the Lissajous figure is typical for dielectric barrier discharge plasma [53]. When the catalyst is introduced into the discharge zone, the input power is decreased Figure 8d. The discharge behavior in the absence of the catalyst differs from the one in the empty reactor due to the change in the dielectric properties of the matter between the inner and the outer electrodes.

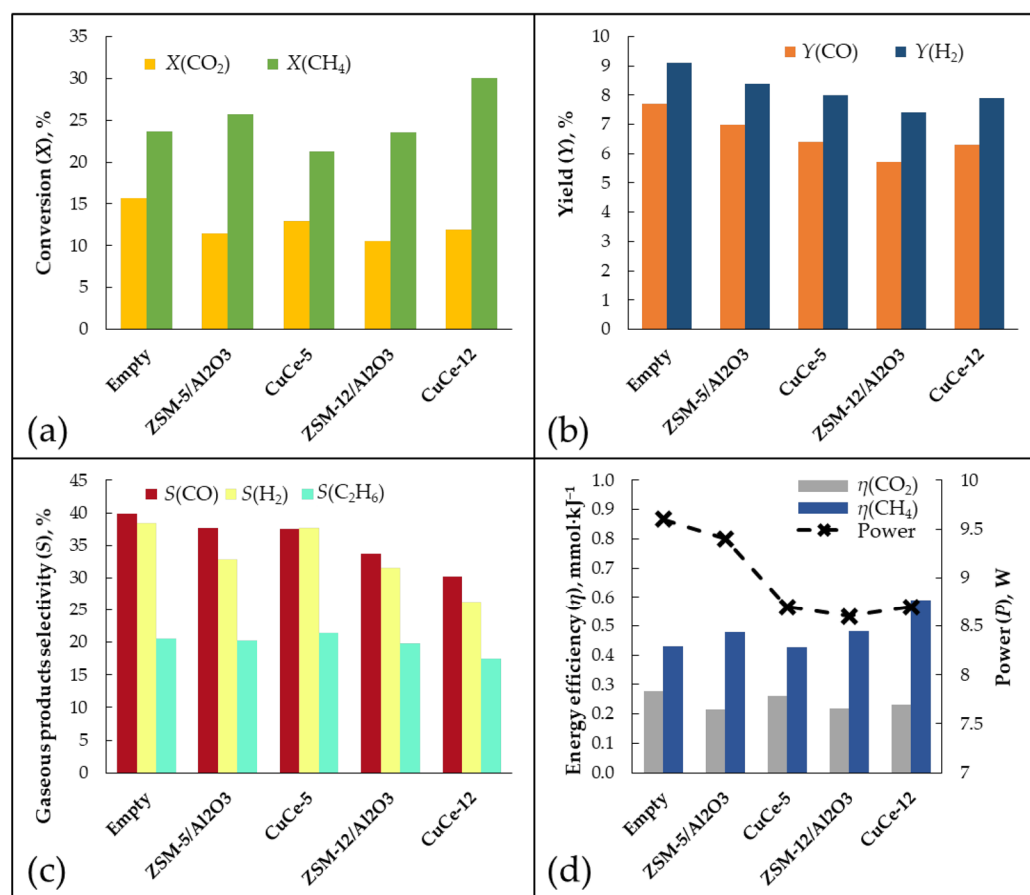


Figure 8. The results of the plasma-catalytic processing of the CH₄ and CO₂ using the prepared catalysts: (a) the conversion of CH₄ and CO₂; (b) yield of the gaseous products; (c) selectivity of the gaseous products; (d) energy efficiency and power.

The supports (ZSM-5/Al₂O₃ and ZSM-12/Al₂O₃) along with the catalysts were also tested in plasma-catalytic CH₄ reforming. From the results, it can be seen that the conversion of CO₂ is decreased when the packing material is introduced. As carbon dioxide is a gas with acidic properties, a less acidic catalyst would be preferable. However, when material with less acidity was present (ZSM-12 based catalyst), no significant change in CO₂ conversion was observed. Apparently, better adsorption would be achieved on strong basic sites which were not determined in the prepared catalysts. A minor increase in the CO₂ conversion was achieved when the CeO₂ was impregnated compared to the pure support. Cerium oxide possesses oxygen vacancies in the structure, which promote the splitting of CO₂ into CO [54]. The conversion of CH₄ increased and was the highest in presence of the CuCe-12 sample. When relating the conversion to the input power, it was seen that in presence of CuCe-5 and CuCe-12, the input power was similar but CH₄ conversion in the presence of CuCe-12 was higher, which is attributed to the synergy between the plasma and the catalyst. The activated methane molecule bridges to the Cu atom with subsequent recombination to gaseous and liquid products. Apparently, the higher surface area and the higher distribution of the CuO species on the CuCe-5 surface did not provide

much of an effect on CH_4 conversion compared to the bigger CuO crystallites in the case of CuCe-12 . The products of $\text{CH}_4\text{-CO}_2$ reforming included H_2 , CO , and C_2H_6 . The yields of the products and their selectivities are presented in Figure 8b,c. It can be seen that the product yields are the highest in the case of an empty reactor, which may be attributed to the higher input power. As was mentioned before, in the presence of packing materials, the consumed power slightly decreases, which may affect product formation. It should be noted that the CuCe-12 sample exhibits the lowest selectivity for gaseous products, which may be related to the formation of liquid products.

The liquid products, which were produced during plasma-catalytic processing of the gases, were collected into a beaker containing distilled water to prevent evaporation. The resulting water solution was subjected to a gas chromatography analysis and the main products, which were methanol and acetone, were determined. From Figure 9 it may be observed that the total quantity of the oxygenated products was the highest in presence of the CeCe-12 catalyst. This is consistent with the suggestion that the decreased selectivity of the gaseous products (H_2 , CO , C_2H_6) is attributed to the formation of liquid products. When comparing the two types of catalysts, it can be seen that more liquid products were produced in the presence of the ZSM-12 -supported catalyst. A possible explanation can be the difference in acid properties. The catalyst with less acid centers promotes the formation of methanol rather than carboxylic acids [38]. During the plasma activation of the $\text{CH}_4\text{-CO}_2$ gas mixture, CO_2^* , CH_4^* , and CO^* excited species are formed as well as CH_3 , CH_2 , CH , H , and O radicals [55]. As a result of species recombination in the plasma and on the surface of the catalyst, OH , HCO_{ads} , $\text{H}_2\text{CO}_{\text{ads}}$, and $\text{H}_3\text{CO}_{\text{ads}}$ are produced, which further transform into molecules like CH_3OH . According to the literature [56], the presence of acetone in the products is attributed to HCO_{ads} species which couple with C_2 species to form a C_3 -intermediate resulting in acetone formation.

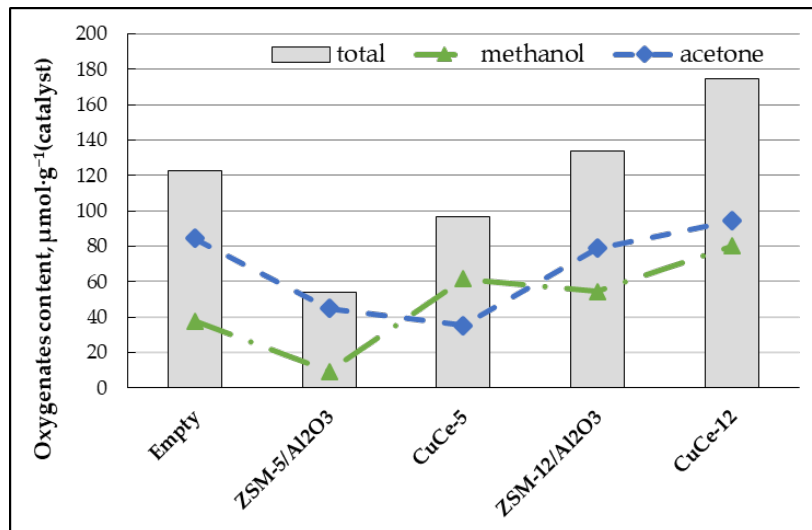


Figure 9. The results of the obtained liquid phase chromatographic analysis.

The results obtained were compared to previously published investigations on plasma-catalytic DRM and CO_2 decomposition (Table 5). It can be seen from the table that in the present work, the conversion of CO_2 and CH_4 was comparable to that in presence of the $\text{Cu}/\text{Al}_2\text{O}_3$ catalyst from the literature [57], but the energy efficiency in our system was considerably higher (0.8 kJ/mmol vs. 0.18 kJ/mmol). It can also be seen that in the major part of the Cu -involving DRM related works, methanol is the main product among the oxygenates produced and in our research, methanol content increases when the ZSM-12 zeolite is introduced into the catalyst composition. It should be noted that the Cu/CeO_2 catalyst from the recent study [38] shows the worst CO_2 conversion results among other catalysts. The authors explain this phenomenon by the interaction of Cu^+ species with

CeO₂ oxygen vacancies, which led to CO + H₂O reaction activation with subsequent CO₂ formation. Thus, controlling the valence state of the Cu species is essential for plasma-catalytic DRM reactions. In contrast, a CuO-based catalyst on CeAl support may lead to 13.5% CO₂ conversion if the CH₄ is absent, which means no side reactions occur. In the presence of our CuCe catalytic systems, the CO₂ conversion is lower due to the acidic nature of the zeolite-containing support.

From the literature, it is known that acetic acid is one of the desired products in plasma-catalytic dry methane reforming. However, in our system, no amount of this acid was observed when analyzing the liquid phase. One of the possible reasons for the absence of acetic acid in the liquid products can be the limited desorption of the acid from the zeolite pores, as reported in the literature [40]. In order to overcome this limitation, reactor modification is needed in future work. For example, reactor cooling or co-reagent injection (such as O₂ or water vapor) may take place.

Reusability tests of the CuCe-12 were carried out in order to investigate the stability of the catalyst. Each run duration was 2 h in order to obtain three samples of the gas. No catalyst pretreatment was made between the runs. It was revealed that the obtained sample was stable in the current conditions within the investigated time (10 h) and no drastic changes in gas conversion and the yields of H₂ and CO were observed (Figure 10). It may be preliminarily concluded that catalyst deactivation did not occur in the present experiment during the 10 h of the total activity of the tests and thus the catalyst may be used in several cycles. The only problem with a continuous run is related to reactor heating, so additional technological solutions need to be implemented in future work.

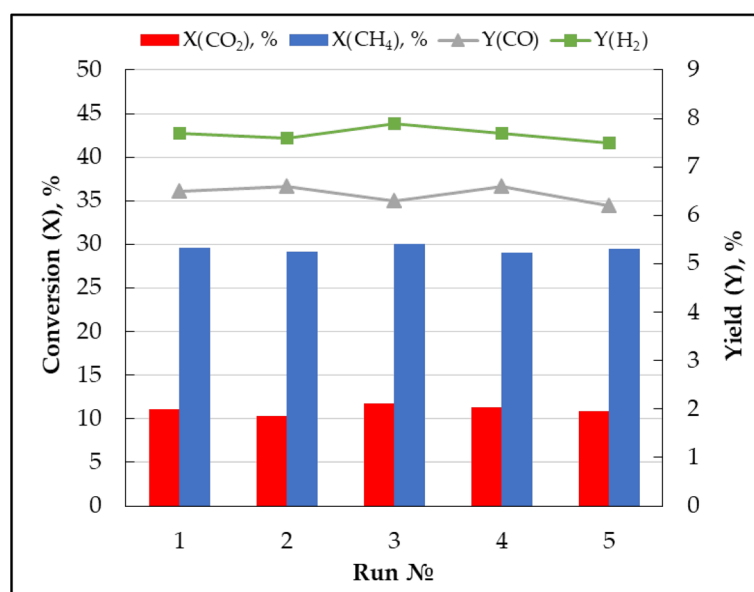


Figure 10. The CuCe-12 catalyst stability test during five runs (Absorbed power = 9 W, CH₄:CO₂ = 1:1, flow rate = 47 mL/min).

Table 5. DBD plasma-catalytic DRM and CO₂ decomposition performance data using Cu catalysts.

Catalyst	Input Power, W	Gas Flow, mL/min	η (Total), mmol·kJ ⁻¹	X (CO ₂), %	X (CH ₄), %	Oxygenates Distribution	Source
Cu/Al ₂ O ₃	10	40	n/d *	7	16	acetic acid, methanol, ethanol, formic acid	[21]
Cu/Al(OH) ₃				6	17	R-OH	
Cu/Mg(OH) ₂				9	19	R-OH	
Cu/SiO ₂	12	40	n/d	7	20	R-OH, R-COOH	[29]
Cu/HZSM-5				9	19	R-OH, R-COOH	
Cu/TiO ₂				4	14	R-OH, R-COOH	
Cu/Al ₂ O ₃	10	40	n/d *	7	16	acetic acid, methanol, ethanol, formic acid	[21]

Table 5. Cont.

Catalyst	Input Power, W	Gas Flow, mL/min	η (Total), mmol·kJ ⁻¹	X (CO ₂), %	X (CH ₄), %	Oxygenates Distribution	Source
Cu/CeO ₂ Cu/TiO ₂ Cu/ γ -Al ₂ O ₃ Cu/Al(OH) ₃	5	40	n/d	1 4 2.5 7	13 5 11 16	methanol, ethanol, Pr-OH, Bu-OH, acetic acid, acetone Cu/CeO ₂ —lowest oxygenates selectivity Cu/Al(OH) ₃ —highest oxygenates selectivity	[38]
Cu/Al ₂ O ₃	45	50	0.18	16	32	methanol, ethanol, DME, formic acid	[57]
Cu/ γ -Al ₂ O ₃	7.5	50	0.56	8	15	n/d	[58]
CuCe-5 CuCe-12	8.7	47	0.65 0.8	12 11	20 30	methanol, acetone	This work
CuO/CeAl CuO/Al ₂ O ₃	2.2	30	1.4 1.6	13.5 15.7	n/a **	n/a	[59]

* n/d = no data, ** n/a = not applicable since only CO₂ decomposition to CO is considered in the study.

4. Conclusions

In the present work, the conversion of greenhouse gases was conducted via the plasma-catalytic dry methane reforming approach using zeolite-containing catalysts. Under the studied conditions, the conversion of CH₄ increases in the presence of the catalysts, but CO₂ conversion slightly decreases which can be explained by the decrease of the input power in the presence of packing material and the acidic properties of the catalysts. Based on analysis results, the ZSM-5-based catalyst (CuCe-5) had a higher specific surface area, higher concentration of acid centers, and better CuO distribution. Nevertheless, CH₄ conversion was higher and liquid phase content increased in the presence of CuCe-12. These effects are related to lower acidity as well as the bulk Cu phase which bridges the CH₃ species and allows them to recombine with CH₃OH and CH₃C(O)CH₃ molecules. There are still challenges to overcome in plasma-catalytic dry methane reforming. The design and optimization of the plasma-catalyst system requires careful consideration of factors such as plasma power, catalyst type, and reactor configuration. Further research and development efforts are ongoing for a better understanding of the complex interactions between plasma and catalysts and to improve the overall performance of this process.

Author Contributions: Conceptualization, A.L.M. and O.V.G.; methodology, O.V.G.; validation, O.V.G. and D.E.T.; investigation, O.V.G.; resources, O.V.G. and D.E.T.; writing—original draft preparation, O.V.G. and D.E.T.; writing—review and editing, A.L.M.; visualization, O.V.G.; supervision, A.L.M.; project administration, O.V.G. All authors have read and agreed to the published version of the manuscript.

Funding: The research was funded by the Russian Science Foundation, grant number 22-79-00259.

Data Availability Statement: Data are contained within the article.

Acknowledgments: The authors thank Golubev K.B. for the chromatographic determination of the liquid samples. This work was performed using the equipment of the Shared Research Center, the Analytical Center of Deep Oil Processing and Petrochemistry of the A.V. Topchiev Institute of Petrochemical Synthesis, RAS.

Conflicts of Interest: The authors declare no conflict of interest.

References

- Kostyuchenko, N.; Smolennikov, D. Greenhouse Gas Emissions. In *Responsible Consumption and Production*; Filho, W.L., Azul, A.M., Brandli, L., Özuyar, P.G., Wall, T., Eds.; Springer: Cham, Switzerland, 2022; pp. 324–335. [\[CrossRef\]](#)
- Lalsare, A.; Sivri, A.; Egan, R.; Vukmanovich, R.J.; Dumitrescu, C.E.; Hu, J. Biomass—Flare gas synergistic co-processing in the presence of carbon dioxide for the controlled production of syngas (H₂:CO~2–2.5). *Chem. Eng. J.* **2020**, *385*, 123783. [\[CrossRef\]](#)
- Cai, X.; Hu, Y.H. Advances in catalytic conversion of methane and carbon dioxide to highly valuable products. *Energy Sci. Eng.* **2019**, *7*, 4–29. [\[CrossRef\]](#)

4. Hussien, A.G.S.; Polychronopoulou, K.A. Review on the Different Aspects and Challenges of the Dry Reforming of Methane (DRM) Reaction. *Nanomaterials* **2022**, *12*, 3400. [[CrossRef](#)] [[PubMed](#)]
5. Lavoie, J.-M. Review on dry reforming of methane, a potentially more environmentally-friendly approach to the increasing natural gas exploitation. *Front. Chem.* **2014**, *2*, 81. [[CrossRef](#)] [[PubMed](#)]
6. An, Y.; Lin, T.; Yu, F.; Yang, Y.; Zhong, L.; Wu, M.; Sun, Y. Advances in direct production of value-added chemicals via syngas conversion. *Sci. China Chem.* **2017**, *60*, 887–903. [[CrossRef](#)]
7. Wender, I. Synthesis Gas as a Source of Fuels and Chemicals: C-1 Chemistry. *Annu. Rev. Energy* **1986**, *11*, 295–314. [[CrossRef](#)]
8. Han, J.W.; Park, J.S.; Choi, M.S.; Lee, H. Uncoupling the size and support effects of Ni catalysts for dry reforming of methane. *Appl. Catal. B* **2017**, *203*, 625–632. [[CrossRef](#)]
9. Jabbour, K.; El Hassan, N.; Davidson, A.; Massiani, P.; Casale, S. Characterizations and performances of Ni/diatomite catalysts for dry reforming of methane. *Chem. Eng. J.* **2015**, *264*, 351–358. [[CrossRef](#)]
10. Zafarnak, S.; Rahimpour, M.R. Co-Ni bimetallic supported on mullite as a promising catalyst for biogas dry reforming toward hydrogen production. *Mol. Catal.* **2023**, *534*, 112803. [[CrossRef](#)]
11. Xu, D.-J.; Wu, J.; Liu, Z.; Qiao, L.-Y.; Zong, S.-S.; Zhou, Z.-F.; Yao, Y.-G. Doping low amount of Zirconium in Rh-LTO to prepare durable catalysts for dry reforming of methane. *Mol. Catal.* **2023**, *535*, 112822. [[CrossRef](#)]
12. Bai, Y.; Sun, K.; Wu, J.; Zhang, M.; Zhao, S.; Kim, Y.D.; Liu, Y.; Gao, J.; Liu, Z.; Peng, Z. The Ga-promoted Ni/CeO₂ catalysts for dry reforming of methane with high stability induced by the enhanced CO₂ activation. *Mol. Catal.* **2022**, *530*, 112577. [[CrossRef](#)]
13. Kushida, M.; Yamaguchi, A.; Miyauchi, M. Photocatalytic dry reforming of methane by rhodium supported monoclinic TiO₂-B nanobelts. *J. Energy Chem.* **2022**, *71*, 562–571. [[CrossRef](#)]
14. Tahir, M.; Ali Khan, A.; Bafaqeer, A.; Kumar, N.; Siraj, M.; Fatehmulla, A. Highly Stable Photocatalytic Dry and Bi-Reforming of Methane with the Role of a Hole Scavenger for Syngas Production over a Defective Co-Doped g-C₃N₄ Nanotexture. *Catalysts* **2023**, *13*, 1140. [[CrossRef](#)]
15. Zhang, Z.-Y.; Li, T.; Yao, J.-L.; Xie, T.; Xiao, Q. Mechanism and kinetic characteristics of photo-thermal dry reforming of methane on Pt/mesoporous-TiO₂ catalyst. *Mol. Catal.* **2023**, *535*, 112828. [[CrossRef](#)]
16. Mehta, P.; Barboun, P.; Go, D.B.; Hicks, J.C.; Schneider, W.F. Catalysis Enabled by Plasma Activation of Strong Chemical Bonds: A Review. *ACS Energy Lett.* **2019**, *4*, 1115–1133. [[CrossRef](#)]
17. Vadikkeettil, Y.; Subramaniam, Y.; Murugan, R.; Ananthapadmanabhan, P.V.; Mostaghimi, J.; Pershin, L.; Batiot-Dupeyrat, C.; Kobayashi, Y. Plasma assisted decomposition and reforming of greenhouse gases: A review of current status and emerging trends. *Renew. Sustain. Energy Rev.* **2022**, *161*, 112343. [[CrossRef](#)]
18. Abiev, R.S.; Sladkovskiy, D.A.; Semikin, K.V.; Murzin, D.Y.; Rebrov, E.V. Non-Thermal Plasma for Process and Energy Intensification in Dry Reforming of Methane. *Catalysts* **2020**, *10*, 1358. [[CrossRef](#)]
19. Malik, M.I.; Achouri, I.E.; Abatzoglou, N.; Gitzhofer, F. Intensified performance of methane dry reforming based on non-thermal plasma technology: Recent progress and key challenges. *Fuel Process. Technol.* **2023**, *245*, 107748. [[CrossRef](#)]
20. Liu, S.; Winter, L.R.; Chen, J.G. Review of Plasma-Assisted Catalysis for Selective Generation of Oxygenates from CO₂ and CH₄. *ACS Catal.* **2020**, *10*, 2855–2871. [[CrossRef](#)]
21. Wang, L.; Yi, Y.; Wu, C.; Guo, H.; Tu, X. One-Step Reforming of CO₂ and CH₄ into High-Value Liquid Chemicals and Fuels at Room Temperature by Plasma-Driven Catalysis. *Angew. Chem. Int. Ed.* **2017**, *56*, 13679–13683. [[CrossRef](#)]
22. Ban, T.; Yu, X.-Y.; Kang, H.-Z.; Zhang, H.-X.; Gao, X.; Huang, Z.-Q.; Chang, C.-R. Design of Single-Atom and Frustrated-Lewis-Pair dual active sites for direct conversion of CH₄ and CO₂ to acetic acid. *J. Catal.* **2022**, *408*, 206–215. [[CrossRef](#)]
23. Lia, D.; Rohania, V.; Fabrya, F.; Ramaswamy, A.P.; Sennourb, M.; Fulcheri, L. Direct conversion of CO₂ and CH₄ into liquid chemicals by plasma-catalysis. *Appl. Catal. B* **2020**, *261*, 118228. [[CrossRef](#)]
24. Puliyalil, H.; Jurkovic, D.L.; Dasireddy, V.D.B.C.; Likoazar, B. A review of plasma-assisted catalytic conversion of gaseous carbon dioxide and methane into value added platform chemicals and fuels. *RSC Adv.* **2018**, *8*, 27481. [[CrossRef](#)] [[PubMed](#)]
25. Shi, C.; Wang, S.; Ge, X.; Deng, S.; Chen, B.; Shen, J. A review of different catalytic systems for dry reforming of methane: Conventional catalysis-alone and plasma-catalytic system. *J. CO₂ Util.* **2021**, *46*, 101462. [[CrossRef](#)]
26. Marinho, A.L.A.; Toniolo, F.S.; Noronha, F.B.; Epron, F.; Duprez, D.; Bion, N. Highly active and stable Ni dispersed on mesoporous CeO₂-Al₂O₃ catalysts for production of syngas by dry reforming of methane. *Appl. Catal. B* **2021**, *281*, 119459. [[CrossRef](#)]
27. Bouchoul, N.; Touati, H.; Fourr'e, E.; Clacens, J.-M.; Batonneau-Gener, I.; Batiot-Dupeyrat, C. Plasma-catalysis coupling for CH₄ and CO₂ conversion over mesoporous macroporous Al₂O₃: Influence of the physico-chemical properties. *Appl. Catal. B* **2021**, *295*, 120262. [[CrossRef](#)]
28. Tao, X.; Yang, C.; Huang, L.; Xu, D. DBD plasma combined with catalysts derived from NiMgAlCe hydrotalcite for CO₂ reforming of CH₄. *Mater. Chem. Phys.* **2020**, *250*, 123118. [[CrossRef](#)]
29. Wang, Y.; Fan, L.; Xu, H.; Du, X.; Xiao, H.; Qian, J.; Zhu, Y.; Tu, X.; Wang, L. Insight into the synthesis of alcohols and acids in plasma-driven conversion of CO₂ and CH₄ over copper-based catalysts. *Appl. Catal. B* **2022**, *315*, 121583. [[CrossRef](#)]
30. Dou, L.; Liu, Y.; Gao, Y.; Li, J.; Hu, X.; Zhang, S.; Ostrikov, K.; Shao, T. Disentangling metallic cobalt sites and oxygen vacancy effects in synergistic plasma-catalytic CO₂/CH₄ conversion into oxygenates. *Appl. Catal. B* **2022**, *318*, 121830. [[CrossRef](#)]

31. Wang, J.; Zhang, K.; Bogaerts, A.; Meynen, V. 3D porous catalysts for Plasma-Catalytic dry reforming of Methane: How does the pore size affect the Plasma-Catalytic Performance? *Chem. Eng. J.* **2023**, *464*, 142574. [[CrossRef](#)]
32. Bouchoul, N.; Fourré, E.; Duarte, A.; Tanchoux, N.; Louste, C.; Batiot-Dupeyrat, C. Plasma-metal oxides coupling for CH₄-CO₂ transformation into syngas and/or hydrocarbons, oxygenates. *Catal. Today* **2021**, *369*, 62–68. [[CrossRef](#)]
33. Li, D.; Rohani, V.; Ramaswamy, A.P.; Sennour, M.; Georgi, F.; Dupont, P.; Fulcheri, L. Orientating the plasma-catalytic conversion of CO₂ and CH₄ toward liquid products by using a composite catalytic bed. *Appl. Catal.* **2023**, *650*, 119015. [[CrossRef](#)]
34. Li, J.; Dou, L.; Gao, Y.; Hei, X.; Yu, F.; Shao, T. Revealing the active sites of the structured Ni-based catalysts for one-step CO₂/CH₄ conversion into oxygenates by plasma-catalysis. *J. CO₂ Util.* **2021**, *52*, 101675. [[CrossRef](#)]
35. Mei, D.; Sun, M.; Li, S.; Zhang, P.; Fang, Z.; Tu, X. Plasma-enabled catalytic dry reforming of CH₄ into syngas, hydrocarbons and oxygenates: Insight into the active metals of γ -Al₂O₃ supported catalysts. *J. CO₂ Util.* **2023**, *67*, 102307. [[CrossRef](#)]
36. Krawczyk, K.; Młotek, M.; Ulejczyk, B.; Schmidt-Szałowski, K. Methane conversion with carbon dioxide in plasma-catalytic system. *Fuel* **2014**, *117*, 608–617. [[CrossRef](#)]
37. Li, J.; Dou, L.; Liu, Y.; Gao, Y.; Hu, X.; Yu, F.; Li, J.; Zhang, S.; Shao, T. One-step plasma reforming of CO₂-CH₄ into hydrogen and liquid fuels: The roles of Cu and Fe sites on products distribution. *Fuel Process. Technol.* **2023**, *242*, 107648. [[CrossRef](#)]
38. Wang, L.; Wang, Y.; Fan, L.; Xu, H.; Liu, B.; Zhang, J.; Zhu, Y.; Tu, X. Direct conversion of CH₄ and CO₂ to alcohols using plasma catalysis over Cu/Al(OH)₃ catalysts. *Chem. Eng. J.* **2023**, *466*, 143347. [[CrossRef](#)]
39. Wang, S.; Guo, S.; Luo, Y.; Qin, Z.; Chen, Y.; Dong, M.; Li, J.; Fan, W.; Wang, J. Direct synthesis of acetic acid from carbon dioxide and methane over Cu-modulated BEA, MFI, MOR and TON zeolites: A density functional theory study. *Catal. Sci. Technol.* **2019**, *9*, 6613. [[CrossRef](#)]
40. Montejo-Valencia, B.D.; Pagán-Torres, Y.J.; Martínez-Iñesta, M.M.; Curet-Arana, M.C. Density Functional Theory (DFT) Study to Unravel the Catalytic Properties of M-Exchanged MFI, (M = Be, Co, Cu, Mg, Mn, Zn) for the Conversion of Methane and Carbon Dioxide to Acetic Acid. *ACS Catal.* **2017**, *7*, 6719–6728. [[CrossRef](#)]
41. Feng, G.; Wen, Z.-H.; Wang, J.; Lu, Z.-H.; Zhou, J.; Zhang, R. Guiding the design of practical MTW zeolite catalysts: An integrated experimental-theoretical perspective. *Microporous Mesoporous Mater.* **2021**, *312*, 110810. [[CrossRef](#)]
42. Golubev, O.V.; Il'chuk, P.S.; Tsaplin, D.E.; Maximov, A.L. Application of Zeolite-Containing Catalysts For Plasma-Catalytic Carbon Dioxide Methane Reforming. *Russ. J. Appl. Chem.* **2022**, *95*, 1749–1755. [[CrossRef](#)]
43. Tsaplin, D.E.; Makeeva, D.A.; Kulikov, L.A.; Maksimov, A.L.; Karakhanov, E.A. Synthesis of ZSM-12 zeolites with new templates based on salts of ethanolamines. *Russ. J. Appl. Chem.* **2018**, *91*, 1957–1962. [[CrossRef](#)]
44. Groen, J.C.; Peffer, L.A.A.; Pérez-Ramírez, J. Pore size determination in modified micro- and mesoporous materials. Pitfalls and limitations in gas adsorption data analysis. *Microporous Mesoporous Mater.* **2003**, *60*, 1–17. [[CrossRef](#)]
45. Sandoval-Díaz, L.-E.; Gonzalez-Amaya, J.-A.; Trujillo, C.-A. General aspects of zeolite acidity characterization. *Microporous Mesoporous Mater.* **2015**, *215*, 229–243. [[CrossRef](#)]
46. Wang, H.; Xu, R.; Jin, Y.; Zhang, R. Zeolite structure effects on Cu active center, SCR performance and stability of Cu-zeolite catalysts. *Catal. Today* **2019**, *327*, 295–307. [[CrossRef](#)]
47. Fedorov, A.V.; Kukushkin, R.G.; Yeletsky, P.M.; Bulavchenko, O.A.; Chesalov, Y.A.; Yakovlev, V.A. Temperature-programmed reduction of model CuO, NiO and mixed CuO-NiO catalysts with hydrogen. *J. Alloys Compd.* **2020**, *844*, 156135. [[CrossRef](#)]
48. Mierczynski, P.; Mierczynska, A.; Ciesielski, R.; Mosinska, M.; Nowosielska, M.; Czyłkowska, A.; Maniukiewicz, W.; Szynkowska, M.I.; Vasilev, K. High Active and Selective Ni/CeO₂-Al₂O₃ and Pd-Ni/CeO₂-Al₂O₃ Catalysts for Oxy-Steam Reforming of Methanol. *Catalysts* **2018**, *8*, 380. [[CrossRef](#)]
49. The Luong, N.; Okumura, H.; Yamasue, E.; Ishihara, K.N. Structure and catalytic behaviour of CuO-CeO₂ prepared by high-energy ball milling. *R. Soc. Open Sci.* **2019**, *6*, 181861. [[CrossRef](#)]
50. Sun, H.; Wang, H.; Qu, Z. Construction of CuO/CeO₂ Catalysts via the Ceria Shape Effect for Selective Catalytic Oxidation of Ammonia. *ACS Catal.* **2023**, *13*, 1077–1088. [[CrossRef](#)]
51. Luo, M.-F.; Zhong, Y.-J.; Yuan, X.-X.; Zheng, X.-M. TPR and TPD studies of CuO/CeO₂ catalysts for low temperature CO oxidation. *Appl. Catal.* **1997**, *162*, 121–131. [[CrossRef](#)]
52. Zhua, P.; Liu, M.; Zhou, R. Effect of interaction between CuO and CeO₂ on the performance of CuO-CeO₂ catalysts for selective oxidation of CO in H₂-rich streams. *Indian J. Chem.* **2012**, *51A*, 1529–1537.
53. Rosenthal, L.A.; Davis, D.A. Electrical Characterization of a Corona Discharge for Surface Treatment. *IEEE Trans. Ind. Appl.* **1975**, *IA-11*, 328–335. [[CrossRef](#)]
54. Golubev, O.V.; Maksimov, A.L. Plasma-Assisted Catalytic Decomposition of Carbon Dioxide. *Russ. J. Appl. Chem.* **2022**, *95*, 617–630. [[CrossRef](#)]
55. Wang, X.L.; Gao, Y.; Zhang, S.; Sun, H.; Li, J.; Shao, T. Nanosecond pulsed plasma assisted dry reforming of CH₄: The effect of plasma operating parameters. *Appl. Energy* **2019**, *243*, 132–144. [[CrossRef](#)]
56. Munir, S.; Varzeghaniab, A.R.; Kaya, S. Electrocatalytic reduction of CO₂ to produce higher alcohols. *Sustain. Energy Fuels* **2018**, *2*, 2532–2541. [[CrossRef](#)]
57. Andersen, J.A.; Christensen, J.M.; Østberg, M.; Bogaerts, A.; Jensen, A.D. Plasma-catalytic dry reforming of methane: Screening of catalytic materials in a coaxial packed-bed DBD reactor. *Chem. Eng. J.* **2020**, *397*, 125519. [[CrossRef](#)]

58. Zeng, Y.; Zhu, X.; Mei, D.; Ashford, B.; Tu, X. Plasma-catalytic dry reforming of methane over γ -Al₂O₃ supported metal catalysts. *Catal. Today* **2015**, *256*, 80–87. [[CrossRef](#)]
59. Ray, D.; Chawdhury, P.; Bhargavi, K.V.S.S.; Thatikonda, S.; Lingaiah, N.; Subrahmanyam, C. Ni and Cu oxide supported γ -Al₂O₃ packed DBD plasma reactor for CO₂ activation. *J. CO₂ Util.* **2021**, *44*, 101400. [[CrossRef](#)]

Disclaimer/Publisher's Note: The statements, opinions and data contained in all publications are solely those of the individual author(s) and contributor(s) and not of MDPI and/or the editor(s). MDPI and/or the editor(s) disclaim responsibility for any injury to people or property resulting from any ideas, methods, instructions or products referred to in the content.